Catalysis Science & Technology

ROYAL SOCIETY OF CHEMISTRY

PAPER

View Article Online
View Journal | View Issue

Cite this: *Catal. Sci. Technol.*, 2025, **15**, 5794

Catalytic valorisation of D-fructose and alcohols using silica–PEI–polyoxometalate composites

Israel T. Pulido-Díaz, [ab] Itzel Guerrero-Ríos *[b] and Dominique Agustin *[ac]

Received 15th April 2025,
Accepted 7th August 2025

DOI: 10.1039/d5cy00465a

rsc.li/catalysis

A nano-catalyst composed of polyoxometalates (POMs) ionically immobilized on polyethyleneimine (PEI) functionalized silica (SiO_2–[PEIH]$_x$[POM]) was used for the dehydration of D-fructose to 5-hydroxymethylfurfural (HMF) and the subsequent oxidation of HMF to 2,5-diformylfuran (DFF). The morphology and textural properties of silica supports, SBA-15 and Stöber nanoparticles, influenced the catalytic outcome. SiO_2–[PEIH]$_x$[POM] demonstrated high thermal stability and exceptional catalytic activity in fructose transformation. Using DMSO as solvent in a one-pot synthesis, we achieved an HMF yield of 95% after 0.5 hours at 150 °C and a DFF yield of 69% after 20 hours, whereas HMF oxidation afforded a DFF yield of 86% under the same conditions with a considerable turnover number (TON) of 1720. These findings suggested that SiO_2–[PEIH]$_x$[POM] catalysts are promising candidates for the valorization of fructose into sustainable chemical sources.

Introduction

The sustainable transition from fossil to renewable chemical sources has driven intensive research into biomass as a valuable feedstock.[1] Furanic-compounds can be obtained from lignocellulose or abundant saccharides, with both sources being promising alternatives to petrochemical sources.[2–6] Representative platform molecules, *e.g.* 5-hydroxymethylfurfural (5-HMF) and furfural,[7,8] can be converted into furan-based monomers and other valuable compounds through oxidative and/or reductive methodologies involving metal-catalysed steps.[3,4,9]

Catalytic transformations of D-fructose into pivotal substrates like 5-HMF and further derivatives stand as versatile platform chemicals for various applications (Scheme 1). 5-HMF can be oxidized to 2,5-diformyl furan (DFF), 5-hydroxymethyl-2-furancarboxylic acid (HMFCA), 5-formyl-2-furan carboxylic acid (FFCA) and furan-dicarboxylic acid (FDCA).[10–12] DFF holds great potential as an intermediate for pharmaceuticals, fungicides, and polymeric materials.[12,13]

Polyoxometalates (POMs), discrete metal–oxygen clusters with redox and acid–base properties, can be exploited for several catalytic methodologies.[14–16] POMs have gained attention as potential catalysts for upgrading biomass into bio-sourced chemicals and -fuels.[17–20] Among the POMs, stable Keggin structures $[X_xM_{12}O_{40}]^{n-}$ are extensively studied.[15] These structures comprise oxygen atoms, one central templating heteroatom (X = Si, P, or B), and addenda atoms (M = Mo, W, or V), typically in a high-valent (d^0 or d^1) electronic configuration. Despite the potential of POMs as catalysts, their high solubility in water and polar organic solvents often complicates their separation and reuse, thereby limiting their practical utility.

In the past decade, POMs have garnered significant attention as catalysts for tandem dehydration–oxidation of D-fructose into DFF, a "one-pot" methodology well-aligned with the principles of green chemistry.[21–24] Direct transformation of carbohydrates into DFF is particularly advantageous since it avoids isolation and purification steps required when synthesized from 5-HMF. Moreover, the selective oxidation of 5-HMF into DFF using molecular oxygen as an oxidant represents a sustainable and cost-effective strategy for biomass valorisation.[15]

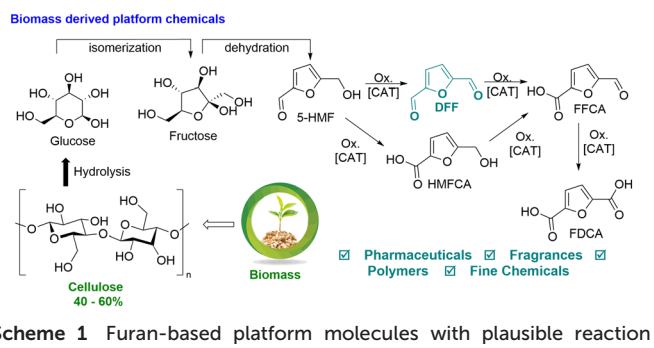

Scheme 1 Furan-based platform molecules with plausible reaction pathways from cellulose.

[a] *Centre National de la Recherche Scientifique (CNRS), Laboratoire de Chimie de Coordination (LCC), Université de Toulouse, UPS, INPT, 205, route de Narbonne, 31077 Toulouse, France. E-mail: dominique.agustin@iut-tlse3.fr*
[b] *Departamento de Química Inorgánica y Nuclear, Facultad de Química, UNAM, Circuito Escolar S/N, Coyoacán, Cd. Universitaria, 04510 Ciudad de México, Mexico. E-mail: itzelgr@unam.mx*
[c] *Université de Toulouse, IUT Toulouse Auch Castres, Département de Chimie, 5 Allée du Martinet, 81100 Castres CEDEX, France*

The first work showcased the catalytic application of a family of homogeneous acidic Keggin HPOMs ($H_3PMo_{12}O_{40}$, $H_4PMo_{11}VO_{40}$, $H_5PMo_{10}V_2O_{40}$, $H_4PW_{11}VO_{40}$, $H_5SiMo_{11}VO_{40}$) in transforming fructose into DFF over 2 h in air at 160 °C in DMSO.[22] $H_3PMo_{12}O_{40}$ (0.5 mol% POM, 160 °C, 6 h) completed a 68% DFF yield from fructose achieving a TON of 236. Partial substitution of H^+ by Cs^+ in those POMs led to insoluble catalytically active phases. The catalyst $Cs_{0.5}H_{2.5}PMo_{12}O_{40}$ (1.6 mol% POM, 160 °C, 4 h) yielded 69% DFF from fructose employing similar reaction conditions and could be reused for five runs with minimal loss of activity. The TON value of 65 of the modified POM was lower than for the acidic form.

Subsequent advances focused on POMs with organic cations such as ammonium, pyridinium, imidazolium-based ionic liquids (ILs), choline, and amine-based polymers.[25,26] The nature of intermolecular interactions (*e.g.*, van der Waals forces, hydrophobic effects, hydrogen bonding, dipole–dipole interactions) between POM and cations enabled fine-tuning of catalytic activity and by-product suppression.[27] For example, the 1-methylimidazole (IM)-functionalized polyoxometalate $HPMo_8V^{VI}_4O_{40}(V^VO)_2[(V^{IV}O)(IM)_4]_2{\cdot}4H_2O{\cdot}(IM)_8$ (9 mol% POM) could oxidize 5-HMF at 100 °C in toluene, achieving a 90% DFF yield with a TON of around 10 over 4 hours. However, when the purity of oxygen was reduced by the use of air as an oxidant, the yield decreased to 75%.[28]

The immobilisation of POMs on inorganic supports has been an effective strategy to face the separation challenges associated with homogeneous POMs. Inorganic supports often enhanced the catalytic activity of POMs by leveraging their intrinsic properties.[17,29–31] It was demonstrated that 1.4 mol% of $(NH_4)_5H_6PV_8Mo_4O_{40}$ supported on hydroxyapatite could catalyse the oxidation of HMF at 130 °C for 10 h, yielding DFF of 72%, with concomitant reduction of V^V into V^{IV}, affording a TON of 12. A tailored reactivity by basic sites in hydroxyapatite was suggested to enhance the selectivity towards DFF.[32]

A key factor in improving POM catalytic performance is tuning redox properties. Studies highlighted the synergistic effects of Mo^{VI}/Mo^V in POM structures, enhancing catalytic efficiency by enabling O_2 activation.[33,34] A remarkable example is the highly reduced giant POM, $(NH_4)_{42}[Mo^{VI}_{72}Mo^V_{60}O_{372}(CH_3COO)_{30}(H_2O)_{72}]$. A 99% DFF yield over 6 hours at 130 °C in DMSO with a TON of 990 was achieved by this POM using only 0.1 mol%. A proton-coupled electron transfer (PCET) mechanism was proposed to explain the selective oxidation.[34]

Silica (SiO_2) is a robust matrix for POM immobilization.[31,35–39] It prevents POM aggregation and enhances thermal stability. Highly organized porosity in a silica support significantly influences mass transfer phenomena and can modulate selectivity by optimizing interaction between reactants and catalysts. However, this aspect is often underexplored.[37]

Moreover, the abundant silanol groups (–Si–OH) on the silica surface not only enable direct immobilization on the silica surface but also allow further functionalization. This dual capability combines the advantages of hybrid composites and solid supports for POM immobilization while tuning properties to enhance catalytic performance.[30,35,40]

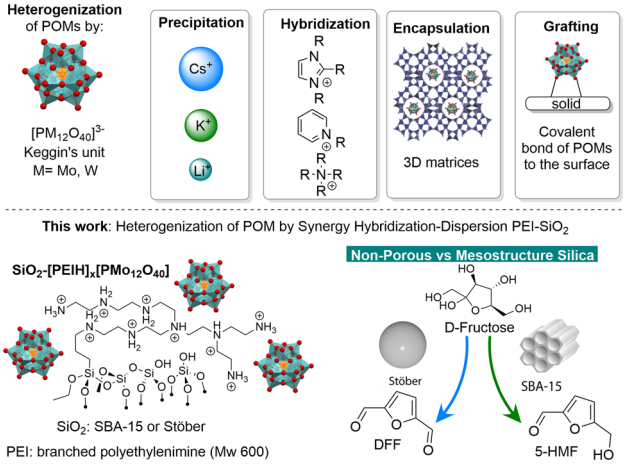

Fig. 1 Different approaches for heterogenization of POMs.

In this study, we report the immobilization of Keggin-type POM $[PMo_{12}O_{40}]^{3-}$ on silica–PEI composites with two distinct textural properties (SBA-15 and Stöber, Fig. 1). The resulting materials were thoroughly characterized and evaluated for the valorisation of D-fructose to DFF and alcohol oxidation.

Results and discussion

Synthesis and characterization of amino-polymer silica composites (SiO_2–PEI)

Mesoporous SBA-15[41] and Stöber[42,43] silica were synthesized and functionalized *via* post-synthetic methodologies.[44] The SiO_2 support was refluxed with (3-chloropropyl)triethoxysilane in dry toluene, then vacuum-dried and reacted with branched PEI_{600} in EtOH/H_2O to obtain SiO_2–PEI materials (see SI Scheme S1).

ATR-IR spectroscopy confirmed the presence of PEI_{600} through C–H vibrations (2800–2990 cm^{-1}) from ethyl and propyl groups.[44] N–H vibrations (3380–3300 cm^{-1}, 1560–1470 cm^{-1}) indicated amino groups,[44,45] while signals at 3300 cm^{-1} (SiO–H) and 1060, 950, 795, and 440 cm^{-1} (Si–O–Si, Si–O) confirmed the silica network (see SI Fig. S1).[45]

The degree of silica functionalization was quantified *via* UDEFT-MAS ^{29}Si NMR (uniform driven equilibrium Fourier transform)[46] revealing T^n signals (−58 ppm, −68 ppm) indicative of covalent silane grafting (Si–CH_2-R, see SI Fig. S2 and S3).[47] Deconvolution allowed calculation of ϕ values (functionalization degree): 0.20 for Stöber–PEI and 0.78 for SBA-15–PEI (see SI Table S1). ^{13}C CP-MAS NMR confirmed PEI incorporation, showing methylene (−57 to −30 ppm) and propyl (−23, −16, −10.5 ppm) signals (see SI Fig. S4 and S5).[48] TGA and elemental analysis revealed comparable PEI_{600} contents for both materials, with Stöber and SBA-15 exhibiting 32 and 37 wt%, respectively (Fig. S6).

Additionally, nitrogen adsorption analysis of SBA-15–PEI (see SI Fig. S7) indicated decreased surface area, pore size,

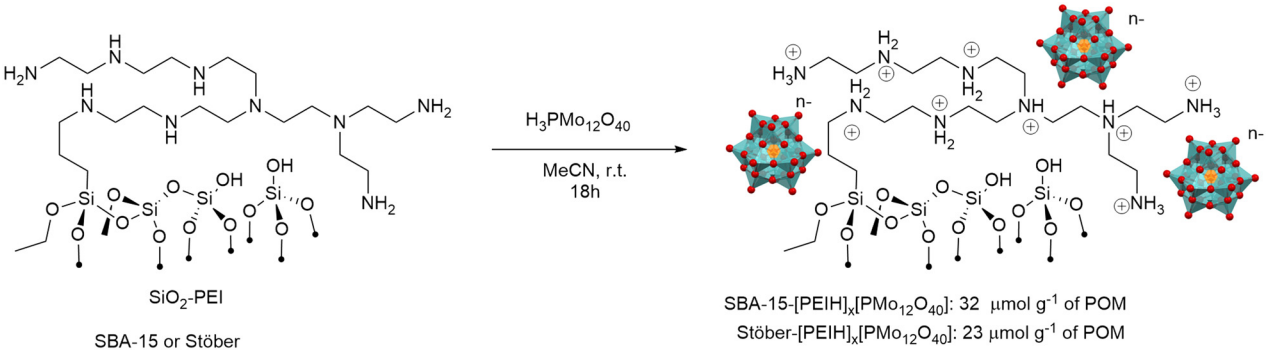

Scheme 2 Synthesis of nanocomposites POM@SiO_2–PEI.

and pore volume evidencing PEI infiltration into the mesopores.

Preparation and characterization of SiO_2–[PEIH]$_x$[POM]

Polyoxometalate $H_3[PMo_{12}O_{40}]$ was immobilized on functionalized silica using a proton exchange approach by mixing silica–PEI and POM in acetonitrile. Upon completion of the reaction, the starting white solid SiO_2–PEI turned blue, indicating the successful immobilization of POMs on silica due to their interaction with the PEI-based material.[49] The recovered material was thoroughly washed with MeCN and water to remove any free POM ions (Scheme 2). ICP-OES analysis of P and MP-AES for Mo confirmed POM loadings of 32 ± 1 μmol on SBA-15 and 23 ± 1 μmol on Stöber-based materials, corresponding to 70 and 48% of the initial polyoxometalate content, respectively (see SI Table S3). The POM nanocomposites were thoroughly characterized using FT-IR, PXRD, solid-state ^{29}Si, ^{13}C, and ^{31}P NMR, EPR and SEM. These analyses confirmed a strong interaction between the support and the POM, driven by electrostatic interactions between the protonated amines of the support and the negatively charged POM ions.

Scanning electron microscopy (SEM) was employed to evaluate the morphology of the POM@SiO_2–PEI materials and to provide an initial assessment of the uniform distribution of POM species across the support surfaces. SEM micrographs did not show significant morphological changes after POM immobilization in SBA-15–PEI (rod-like, Fig. 2A and B) and Stöber–PEI (spherical, Fig. 2G and H) composites. Energy

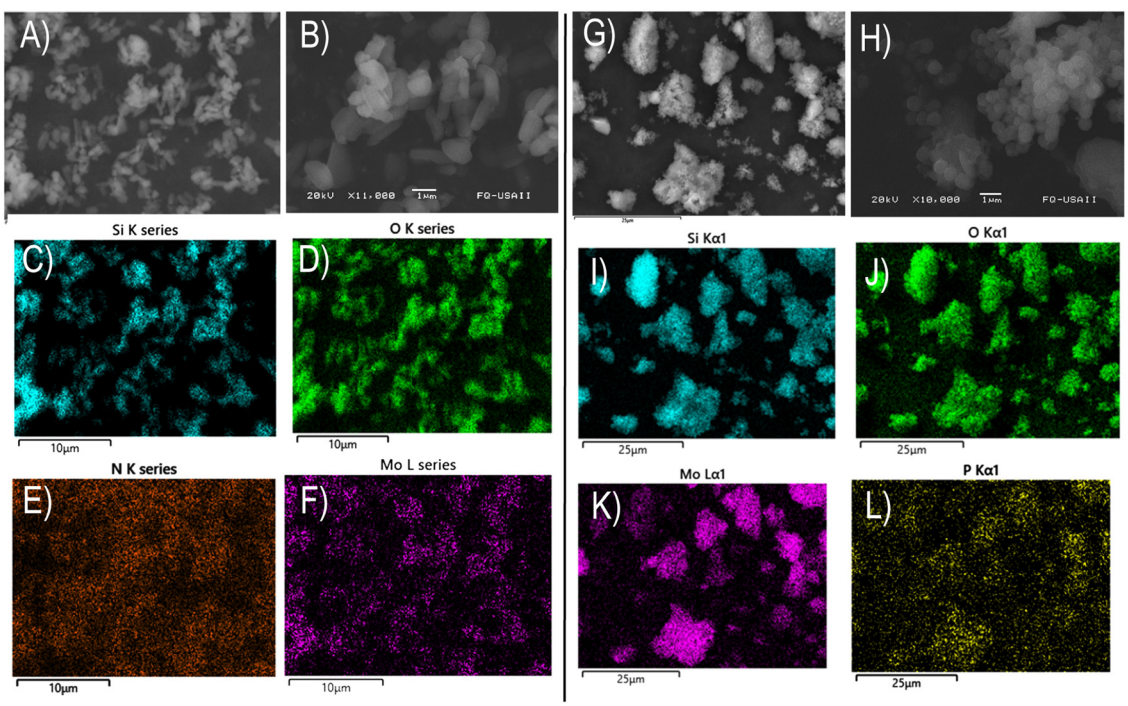

Fig. 2 SEM micrographs of as-synthesized materials. SBA-15–[PEIH$_x$][$PMo_{12}O_{40}$] (low-magnification (A), high-magnification (B), EDS element mapping of Si (C), O (D), N (E) and Mo (F)) and Stöber–[PEIH$_x$][$PMo_{12}O_{40}$] (low-magnification (G), high-magnification (H), EDX element mapping of Si (I), O (J), Mo (K) and P (L)).

dispersive X-ray spectrometry (EDX) confirmed the presence of molybdenum, phosphorus, and nitrogen, indicating successful POM fixation into the SiO_2–PEI materials. Additionally, EDS elemental mapping revealed uniform distribution of molybdenum across the composites.

Powder X-ray diffraction (PXRD) of SiO_2–$[PEIH_x][POM]$ showed loss of crystallinity of original acidic $H_3PMo_{12}O_{40}$ indicating uniform dispersion of POM anions across the silica surface. Complementarily, the PXRD spectra showed the expected amorphous SiO_2 phase with a large diffraction at 23° 2θ (see SI Fig. S8). The ^{13}C CP-MAS NMR spectra (see SI Fig. S9) of SiO_2–$[PEIH_x][PMo_{12}O_{40}]$ materials (SBA-15 and Stöber) displayed resonances for PEI methylene groups ($-CH_2-$) at 57–30 ppm (ref. 48) and propyl silane at 21, 16 and 10 ppm, confirming that the organic framework remained unchanged after POM anchoring.

The ^{29}Si MAS UDEFT NMR spectra (Fig. 3 and SI Table S1) of both materials showed characteristic Q^n resonances at −94 ppm (Q^2), −102 ppm (Q^3) and −111 ppm (Q^4), along with T^n signals at −57 ppm (T^2) and −67 ppm (T^3). Notably, after POM immobilization, the T^2 signal decreased while the T^3 signal increased, suggesting that the acidity of $H_3PMo_{12}O_{40}$ promoted further condensation of the ethoxy groups in the SiO_2–PEI materials, enhancing their integration with the silica matrix.

Solid-state ^{31}P CP-MAS NMR (Fig. 4A) analysis revealed the presence of two primary phosphorus species: a broad signal at

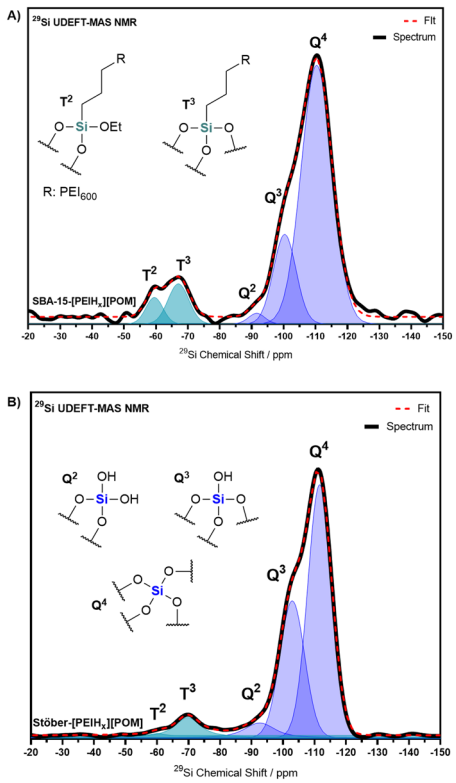

Fig. 3 ^{29}Si UDEFT NMR spectra of a) SBA-15–$[PEIH_x][POM]$ (A) and Stöber–$[PEIH_x][POM]$ (B), with inset of structures of Si species observed (T^n: carbon-bonded silicon atoms, Q^n: silanols and siloxanes).

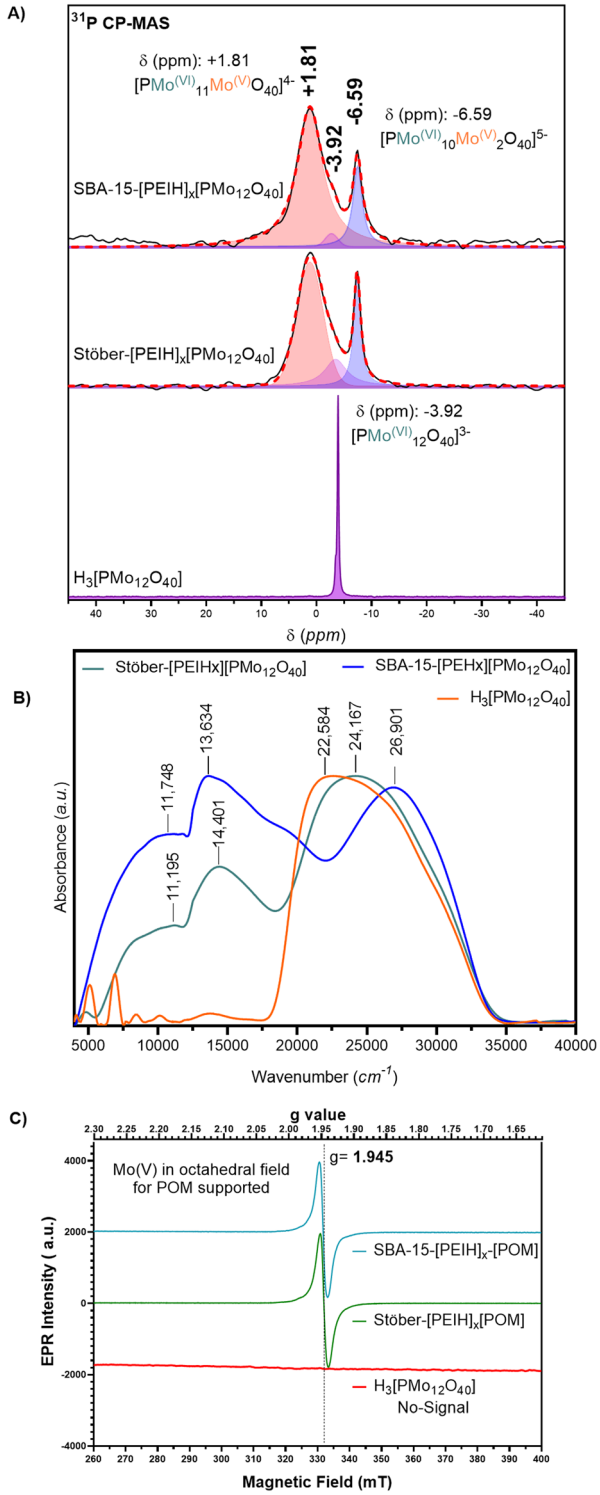

Fig. 4 Spectroscopic characterization of SiO_2–$[PEIH_x][PMo_{12}O_{40}]$. A) ^{31}P CP-MAS NMR spectra, B) diffuse reflectance ultraviolet-visible-near infrared spectra, and C) solid state EPR spectra of Mo(v) cations embedded in supported POM clusters at 77 K.

+1.81 ppm, attributed to paramagnetic one-electron-reduced $[PMo^{(VI)}{}_{11}Mo^{(V)}O_{40}]^{4-}$ clusters, and a sharp signal at −6.59 ppm corresponding to diamagnetic two-electron-reduced $[PMo^{(VI)}{}_{10}Mo^{(V)}{}_2O_{40}]^{5-}$.[50–52] Additionally, a shoulder at around −3.92 ppm

was present in the spectra, assigned to non-reduced species $[PMo^{(VI)}_{12}O_{40}]^{3-}$ as shown in the acquired spectra of the acidic $H_3[PMo_{12}O_{40}]\cdot xH_2O$ compound.

The electronic structure of $[PMo_{12}O_{40}]^{n-}$ clusters attached to SiO_2–PEI was further examined using diffuse reflectance ultraviolet-visible-near infrared (UV/vis/NIR) spectroscopy (Fig. 4B). The acidic $H_3[PMo_{12}O_{40}]\cdot xH_2O$ exhibited characteristic broad absorption peaks at 22 584 cm^{-1} (442 nm) and a shoulder at 26 767 cm^{-1} (373 nm), corresponding to $O^{2-} \rightarrow Mo^{6+}$ charge transfer in Mo═O and Mo–O–Mo bonds.[53] Interestingly, in SBA-15, these transitions shifted to higher energy, likely due to cluster confinement within mesopores.[54] Further evidence for the partially reduced form of POM clusters supported in SiO_2–PEI was observed from two absorption bands at around 13 401 cm^{-1} (764 nm) and 11 748 cm^{-1} (851 nm), which can be assigned to the d–d transition of the Mo(v) octahedron and the Mo(v)-to-Mo(vi) intervalence transition within $[PMo_{12}O_{40}]^{n-}$, respectively.[53,55]

The EPR spectra (Fig. 4C) at 77 K confirmed the existence of Mo(v) species[53,55,56] with a signal centred at $g = 1.95$. The Mo^{5+} cations reside in octahedral symmetry sites, as evidenced by an isotropic signal. Interestingly, no hyperfine structure was observed, suggesting negligible contribution from ^{95}Mo and ^{97}Mo isotopes (both with nuclear spin $I = 5/2$) (Fig. 4B).[55]

The partial reduction of POM species forming mixed-valence Mo(vi)/Mo(v) complexes arises from the photochromic effect induced by primary and secondary amines.[53,57,58] This process begins with the initial reduction step where the Mo(vi) centre forms an intermediate structure featuring a single unshared oxo ligand. This configuration occurs when a terminal oxygen ligand relocates to a bridging position within the molecular framework. EPR data are consistent with an electron localized on the octahedral $\{Mo(v)O_5(OH)\}$ site resulting from electron transfer between the POM and $[NH_3R]^+$ through hydrogen bonding.[55]

The performance of the SiO_2–$[PEIH]_x$[POM] composite system was assessed in the tandem conversion of D-fructose to DFF. Key reaction parameters were evaluated and their impact on DFF formation is detailed in the following section.

Catalytic one-pot dehydration–oxidation of D-fructose to 5-HMF and DFF

The SiO_2–$[PEIH]_x$[POM] hybrid materials synthesized on Stöber (non-porous) and SBA-15 (mesoporous) were tested in the tandem dehydration–oxidation of D-fructose into DFF. Reactions employed a one-pot/one step protocol under optimized conditions (150 °C, in DMSO, in air and for 5 h). The setup leverages the dual role of DMSO, acting as a solvent and mild oxidant using O_2 from air for the final oxidative aromatization step (Fig. 5).

Influence of catalyst loading at 5 h. The performance of both SBA-15–$[PEIH]_x$[POM] and Stöber–$[PEIH]_x$[POM] catalysts was evaluated across different loading conditions. At low catalyst loadings (5.63 wt%, corresponding to 0.025 mol% POM), both systems achieved high yields of 5-hydroxymethylfurfural (5-HMF),

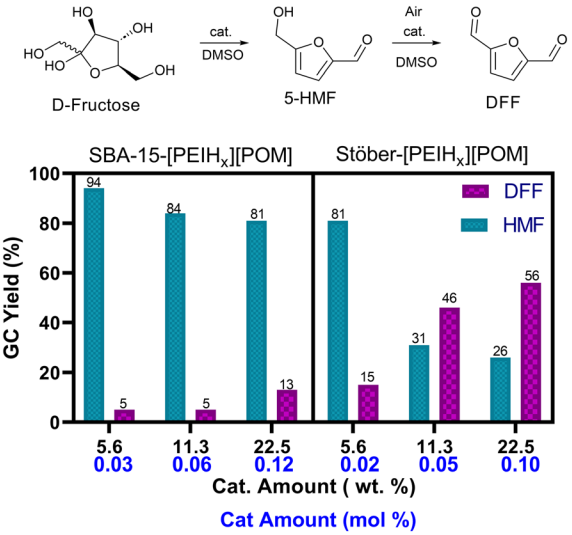

Fig. 5 Initial investigation of SiO_2–$[PEIH]_x$[POM] in D-fructose valorisation. Reaction conditions: 200 mg of D-fructose (1.11 mmol), 5.63, 11.25 or 22.50 wt% (11.3, 22.5 or 45 mg, 0.2–0.12 mol% POM) of the nanocomposite material, 6 mL of DMSO, 150 °C, 5 h, in air. Yields of 5-HMF and DFF were determined by GC-FID employing naphthalene as the internal standard with ±4% variability. Full conversion of fructose after 1 h was checked by ^1H NMR spectroscopy.

while 2,5-diformylfuran (DFF) yields remained below 15%. This outcome is attributed to the Brønsted acidity of the catalysts, predominantly promoting the dehydration of fructose to 5-HMF.[59] In comparison with a blank reaction, DMSO was confirmed to act as both a solvent and a dehydration agent, consistent with previous findings.[60,61]

However, when the catalyst loading was increased to 22.50 wt% (0.10 mol% POM), the SBA-15 supported catalyst showed a low conversion efficiency from 5-HMF to DFF. The low DFF yield of 13% indicated limitations on the oxidative step.

Interestingly, Stöber–$[PEIH]_x$[POM] demonstrated a higher DFF yield (56%) at 22.50 wt% (0.10 mol% POM, TON 580, TOF 116 h^{-1}). ^1H NMR analysis of the reaction mixture revealed carboxylic acid formation (combined yield of formic and acetic acids <10%) and no levulinic acid detected. This product distribution confirms that acid generation arises primarily from direct fructose decomposition rather than secondary 5-HMF rehydration pathways.[62,63] Notably, when the reaction temperature was reduced to 100 °C employing the Stöber–$[PEIH]_x$[POM] catalyst, DFF production became negligible, demonstrating the critical temperature dependence of the oxidation step (see SI Fig. S13).

To further assess the catalytic activity of POM-based materials, control reactions were performed under the same conditions (Fig. 6). Control experiments using only PEI and SBA-15–PEI (11.25 wt%) showed no catalytic activity toward DFF formation, and cannot be differentiated from blank reactions, confirming that the catalytic oxidation is associated with the POM presence.

In contrast with SiO_2–$[PEIH]_x$[POM] hybrid materials, $H_3[PMo_{12}O_{40}]$ was evaluated using 11.25 wt% catalyst loading

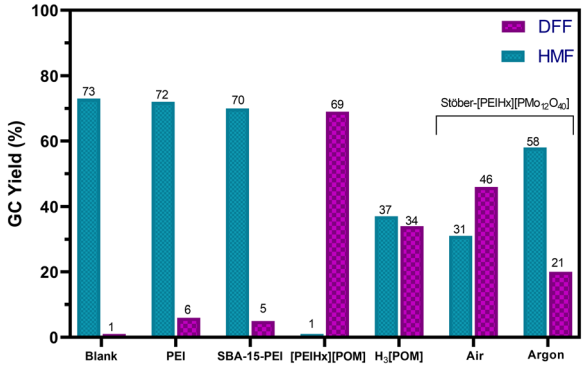

Fig. 6 Blank reaction comparison with SiO_2–$[PEIH]_x[POM]$ in D-fructose valorisation. Reaction conditions: 200 mg of D-fructose (1.11 mmol), silica materials: 11.25 wt% (22.5 mg) of material for SBA-15–$[PEIH]_x[PMo_{12}O_{40}]$ (0.06 mol% $[PMo_{12}O_{40}]$, 0.7 mol% Mo), for Stöber–$[PEIH]_x$[PMo12O40] (0.05 mol%, $PMo_{12}O_{40}$, 0.6 mol% Mo), for $H_3[PMo_{12}O_{40}]$ and hybrid $[PEIH_x][POM]$ materials (0.9 mol% POM), and 6 mL of DMSO, 150 °C, 5 h, in air. Yields of 5-HMF and DFF were determined by GC-FID employing naphthalene as the internal standard with ±4% variability. Full conversion of fructose after 1 h was checked by ^{1}H NMR spectroscopy.

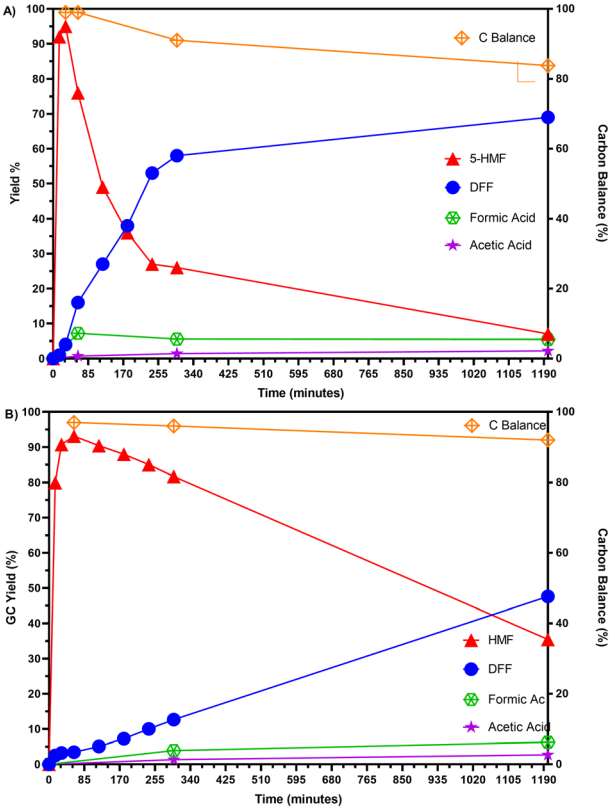

Fig. 7 The distribution of products *versus* reaction time employing A) Stöber–$[PEIH_x][PMo_{12}O_{40}]$ or B) SBA-15–$[PEIH_x][PMo_{12}O_{40}]$ in valorisation of D-fructose. Reaction conditions: 200 mg of D-fructose (1.11 mmol), 45 mg of Stöber or SBA-15–$[PEIH]_x[PMo_{12}O_{40}]$ (22.5 wt%, 0.10 mol%, $PMo_{12}O_{40}$, 1.2 mol% Mo), 6 mL of solvent, 65 mg of naphthalene as the internal standard. HMF and DFF yields were determined by GC-FID; the acid concentration was determined by ^{1}H NMR (400 MHz) using naphthalene as the internal standard.

(0.9 mol%, 0.01 mmol POM) under the same reaction conditions (Fig. 6 and Table S4 in the SI). Despite its higher POM concentration, $H_3[PMo_{12}O_{40}]$ yielded DFF moderately (34%). The reaction mixture showed formic acid (7%) as a side product. For comparison, a non-supported hybrid composite, $[PEIH_x][PMo_{12}O_{40}]$ was synthesized (see SI Fig. S13–S19 for details), and tested under the same conditions (0.9 mol% POM). This heterogeneous composite reached a significantly higher DFF yield (69%). Both Stöber–$[PEIH]_x[POM]$ and non-supported $[PEIH_x][PMo_{12}O_{40}]$ catalysts exhibited higher DFF yields compared to the acidic $H_3[PMo_{12}O_{40}]$. This enhanced performance can be attributed to the synergistic effects of Mo^{6+}/Mo^{5+} within these POM structures, which facilitated O_2 activation. Notably, the presence of approximately 85% Mo(v) content, as estimated by deconvolution of ^{31}P NMR signals, has to be correlated with higher DFF yields compared to fully oxidized $H_3[PMo_{12}O_{40}]$. This suggests that Mo(v) species play a crucial role in promoting 5-HMF oxidation.[33,34] Additionally, factors such as the distribution of Brønsted acid sites and Lewis basic sites may also influence 5-HMF conversion and product selectivity. For POM catalysts, surface oxygen species are another critical factor, known to initiate oxidation reactions, independent of atmospheric oxygen.[33] This is supported by the observation that a certain amount of DFF can still be produced over Stöber–$[PEIH_x][PMo_{12}O_{40}]$ even under an argon atmosphere employing degassed and dry DMSO. Moreover, the reduced catalyst generated during 5-HMF oxidation can be re-oxidized by molecular oxygen, thereby completing the catalytic cycle. This spatio-temporal separation between substrate oxidation and catalyst regeneration underlies the high selectivity toward DFF.[15]

Long-term behaviour of the catalysed one-pot synthesis of DFF from D-fructose. The synthesis of DFF from D-fructose catalysed by Stöber–$[PEIH_x][PMo_{12}O_{40}]$ was investigated by a one-pot/one step protocol. As shown in Fig. 7A, D-fructose was completely converted to 5-HMF, DFF, and acids (formic acid and acetic acid) with a carbon balance of 83% in 20 h. 5-HMF reached a maximum yield of 95% in only 30 min and was further transformed into DFF by continuous heating at 150 °C for another 19 h. The yield of DFF increased with reaction time up to 69% yield in 20 h (TON of 690). Formic acid, a main by-product, was also detected with a yield of 6–7%. When the reaction was completed, the mixture exhibited a brown coloration, indicating humin formation. The presence of humins can indeed account for the observed decrease in carbon balance over time, as previously noted.[30] Being insoluble complex polymers, humins can sequester carbon from the reaction mixture, thereby reducing the overall carbon recovery into desired products.

In the case of SBA-15–$[PEIH]_x[PMo_{12}O_{40}]$, rapid production of 5-HMF is observed at short reaction times. However, the subsequent transformation into DFF proceeds more slowly compared to the Stöber-based material. To assess whether O_2 diffusion into the pores acts as a limiting factor, experiments under pressure were conducted (see SI Table S4, entries 2 and 3). Under 3 bar of synthetic air (20% O_2, 80% N_2), after 5 hours, a modest increase in the DFF yield was observed,

reaching 17% compared to 5% under atmospheric oxygen. However, an unexpected outcome emerged when switching to 3 bar of pure O_2: the DFF yield decreased to 11%, while the formic acid yield increased to 16%. These results suggest that O_2 diffusion is not the primary reason for the slower transformation of intermediates into DFF.

Case of Stöber–$[PEIH]_x[PMo_{12}O_{40}]$ catalysts

Test of heterogeneity of the catalyst and recycling. To assess the stability and potential leaching of $[PMo_{12}O_{40}]^{n-}$, a hot filtration method was used. After 1 hour of reaction at 150 °C, the catalyst was filtered using a 0.45 μm PTFE syringe filter. As shown in Fig. 8, DFF production dramatically dropped post-filtration, indicating few remaining catalysts in the reaction. ICP-OES analysis revealed a minimal amount of Mo (16 ppm) in the organic phase, 7.5% of the initial Mo content. This demonstrates the minimal leaching under high temperature conditions.

Recycling tests were conducted on Stöber–$[PEIH]_x[PMo_{12}O_{40}]$ for the transformation of D-fructose into DFF (Fig. 9). The catalyst demonstrated effective recyclability over four cycles with activity loss after 3 runs. ICP-OES analysis of the reaction solution at the 4th cycle showed a Mo leaching of 55 ppm, equivalent to 26% Mo initial content. This fact could explain the reduced activity observed in the 4th run.

The ATR-IR spectrum of the recovered solid after recycling confirmed that the catalyst structure remained unchanged, with non-appreciable 5-HMF product adsorption (see SI Fig. S15). SEM micrographs with EDS mapping also showed retained structural integrity and uniform Mo dispersion on the silica surface (SI, Fig. S16). Although the IR spectrum indicated no fructose or 5-HMF buildup on the catalyst, the solid-state ^{13}C NMR spectrum of the spent catalyst (SI, Fig. S17) revealed new signals arising from by-products. The peak

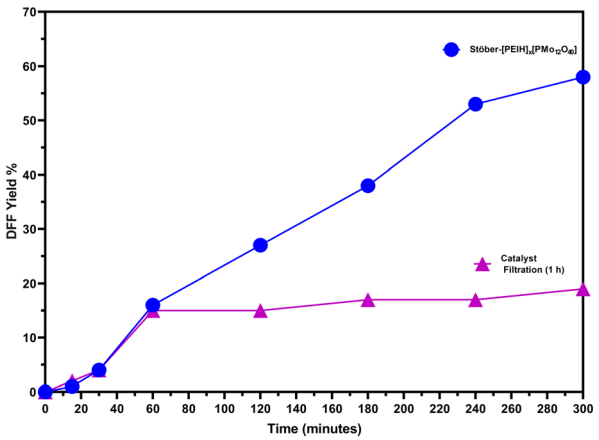

Fig. 8 The leaching test for Stöber–$[PEIH_x][PMo_{12}O_{40}]$ in valorisation of D-fructose. Reaction conditions: 200 mg of D-fructose (1.11 mmol), 45 mg of Stöber–$[PEIH]_x[PMo_{12}O_{40}]$ (22.6 wt%, 0.10 mol%, $PMo_{12}O_{40}$, 1.2 mol% Mo). The catalyst was removed using a syringe filter (PP, GF/D, 2.7 μm) at 150 °C.

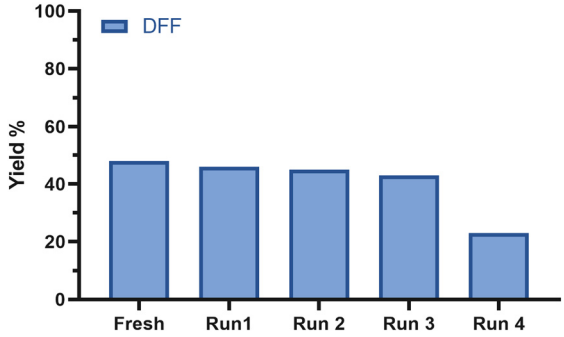

Fig. 9 Recycling experiments for the D-fructose dehydration–oxidation. Reaction conditions: 200 mg of D-fructose (1.11 mmol), 11.25 wt% (22.5 mg) of Stöber–$[PEIH_x][PMo_{12}O_{40}]$, 6 mL of DMSO, 150 °C, 5 h, in air. Yields of 5-HMF and DFF were determined by GC-FID employing naphthalene as the internal standard with ±4% variability. Full conversion of fructose after 1 h was checked by ^1H NMR spectroscopy. The catalyst was recovered by centrifugation at 4000 rpm for 30 min, washed with MeCN twice and dried under vacuum at 90 °C overnight.

at around 39 ppm corresponds to adsorbed DMSO, while signals between 110 and 190 ppm suggest the presence of humins, polymerization by-products of D-fructose and 5-HMF. Humins are categorized into three spectral domains:[64] region I (110–140 ppm) for sp^2 carbons more specifically to β-carbons in furan rings, region II (140–160 ppm) for α-carbons in furan rings, and region III (170–190 ppm) indicating carboxylic acids (notably at 175 ppm). Adsorbed humins can block active sites in the $[PMo_{12}O_{40}]^{n-}$ cluster and account for the activity loss.

The electronic state of the catalyst after the reaction was investigated using diffuse reflectance spectroscopy and solid-state ^{31}P CP-MAS NMR (see SI Fig. S18 and S19). The ^{31}P NMR spectrum revealed the disappearance of signals associated with reduced POM clusters, with the dominant signal at −3.94 ppm corresponding to $[PMo_{12}O_{40}]^{3-}$. However, a residual signal at +0.56 ppm was also observed, which may indicate the presence of partially reduced clusters (Mo(V)). Further evidence for the partially reduced state of the POMs in the spent catalyst was provided by diffuse reflectance spectroscopy, which showed two absorption bands at 13 375 cm^{-1} (747 nm) and 8335 cm^{-1} (1199 nm). These bands, however, appeared with much lower intensity compared to those in the fresh catalyst. These findings suggest that, by the end of the reaction, the majority of the POM catalyst exists in the fully oxidized Mo(VI) state, with only trace amounts of reduced POM clusters remaining.

Direct oxidation of 5-HMF. Given the notable reactivity of SiO_2–$[PEIH]_x[POM]$ in the transformation of fructose to DFF, the direct conversion of 5-HMF to DFF was explored. Moderate conversion was achieved within 5 hours, with high selectivity towards DFF (Scheme 3). The reactivity trend followed: Stöber–$[PEIH]_x[PMo_{12}O_{40}]$ > SBA-15–$[PEIH]_x[PMo_{12}O_{40}]$ > $[PEIH]_x[PMo_{12}O_{40}]$. This confirms the superior reactivity of the Stöber-based material, attributed to the synergistic effects of dispersion on the non-confined silica

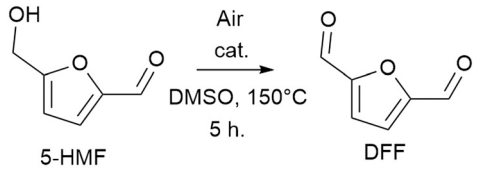

Cat.	Conv. % (Sel.%)
Stöber-[PEIHx][POM]	65 (87)
SBA-15-[PEIHx][POM]	48 (80)
[PEIHx][POM]	50 (40)

Scheme 3 Direct oxidation of 5-HMF catalysed by SiO_2–[$PEIH_x$][POM]. Reaction conditions: 140 mg of 5-HMF (1.11 mmol), 22.5 mg of SBA-15–[$PEIH]_x[PMo_{12}O_{40}$] (0.06 mol% [$PMo_{12}O_{40}$], 0.7 mol% Mo), 22.5 mg of Stöber–[$PEIH]_x[PMo_{12}O_{40}$] (0.05 mol%, $PMo_{12}O_{40}$, 0.6 mol% Mo) or 1.2 mg of [$PEIH]_x[PMo_{12}O_{40}$] (0.05 mol%, $PMo_{12}O_{40}$, 0.6 mol% Mo), 6 mL of solvent, 65 mg of naphthalene as the internal standard. Conversion and selectivity were determined by GC-FID.

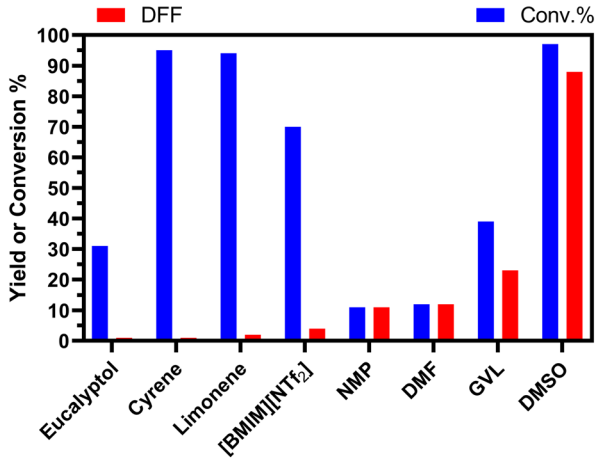

Fig. 10 Solvent screening of direct 5-HMF oxidation employing Stöber–[PEIH]$_x$[PMo12O40] (11.3 wt%, 0.05 mol% $PMo_{12}O_{40}$, 0.6 mol% Mo). Reaction conditions: 0.22 mmol substrate, 4.5 mg Stöber–[$PEIH]_x[PMo_{12}O_{40}$] (0.05 mol% $PMo_{12}O_{40}$, 0.55 mol% Mo), 1.2 mL of solvent, 6.5 mg of naphthalene as the internal standard. Conv. and yields were determined by GC.

surface and the Mo(V)/Mo(VI) redox couple's efficacy in alcohol oxidation.

Notably, when using Stöber–[$PEIH]_x[PMo_{12}O_{40}$] as a catalyst, DFF was not over-oxidized to furfural carboxylic acid (FFCA) or furan-2,5-dicarboxylic acid (FDCA) (Scheme 4). In fact, only 7% conversion to FFCA and FDCA was observed when DFF was used as a substrate at 150 °C for 5 hours (see SI Fig. S21). This outcome highlights the catalyst's ability to selectively oxidize 5-HMF to DFF without further over-oxidation.

When the reaction time increased to 20 h using the Stöber–[$PEIH_x$][POM] catalyst, a DFF yield of 86% and a remarkable TON of 1720 were achieved. Compared with the literature, we achieve the highest TON among several Mo based catalysts (see SI Table S6) for the conversion of 5-HMF as well as D-fructose, with negligible acid formation and carbon balance of 93%. This outcome suggests that water produced during fructose dehydration and fructose itself significantly contribute to humin and acid formation as observed in the one-pot/one-step followed protocol. From

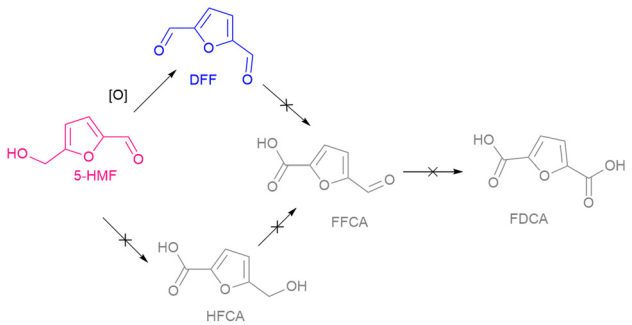

Scheme 4 Possible subproducts of oxidation of 5-HMF; we confirmed that no over-oxidized products were obtained employing the Stöber–[$PEIH]_x[PMo_{12}O_{40}$] material.

D-fructose employing water as a solvent (see SI Table S4, entry 8) after 20 h at 150 °C, only 48% of fructose was converted, a dark-brown precipitate appeared and no DFF was observed.

The solvent polarity was critical in the oxidation of 5-HMF to DFF, as shown in Fig. 10 and Table S5. Non-polar solvents such as eucalyptol (ε = 4.84), cyrene (ε = 3.4), and limonene (ε = 2.4) exhibited low DFF yields (1–2%) despite moderate to high 5-HMF conversions (31–95%), and no other products in the organic phase were detected by GC-MS, probably due to polymerization of HMF at high temperatures (as we observed a black precipitate at the end of the reaction) which are greatly favoured in polar aprotic solvents.[65] Moreover, results suggest that their low polarity hinders the stabilization of polar intermediates or transition states essential for DFF formation. In contrast, polar aprotic solvents like DMSO (ε = 46.7) and DMF (ε = 38.3) showed significantly higher DFF yields (88% and 12%, respectively), with DMSO achieving both the highest conversion (97%) and yield. This underscores the importance of solvent polarity in facilitating the oxidation process, likely due to enhanced solvation of ionic or polar species involved in the reaction mechanism. Interestingly, γ-valerolactone (GVL) (ε = 36.5), despite its relatively high polarity, yielded only moderate DFF production (23%), indicating that factors besides the dielectric constant, such as the solvent structure or specific interactions with the catalyst, may also influence the reaction. In fact, GVL can suffer from ring opening in the presence of primary and secondary amines,[66] so the GVL reaction with polyethyleneimine in the support could eventually hampered the reactivity of PEI–POM species. These results suggest that solvents with higher dielectric constants, particularly DMSO, are more effective in promoting 5-HMF oxidation to DFF, likely due to their ability to stabilize reactive intermediates and enhance catalytic activity.

The active role of DMSO in oxidation reactions has been previously documented by Neumann *et al.*[67] In his work, DMSO acts as an oxygen donor for the oxidation of benzylic alcohol catalysed by $H_3PMo_{12}O_{40}$. The proposed mechanism involves: (a) activation of the sulfoxide through complexation with the polyoxometalate and (b) oxygen transfer from the activated sulfoxide followed by water elimination from the alcohol. In our study, traces of dimethyl sulphide (*m*/*z* 62, Fig. S22) were detected by GC-MS, supporting the participation of DMSO in the reaction. However, alternative mechanisms, such as a proton-coupled electron transfer (PCET) mechanism,[33,34] could also be operative. PCET mechanisms are often challenging to elucidate experimentally due to their complexity,[68] and herein, both pathways—oxygen transfer from DMSO and PCET—could potentially contribute to the selective oxidation of 5-HMF to DFF.

Extension towards alcohol oxidation. With these findings, we also tested the catalyst's efficiency for alcohol oxidation (Scheme 5). The results showed successful oxidation of several primary alcohols to aldehydes with high selectivity and yields (Scheme 5, entries A–D). In the case of perillyl alcohol (Scheme 5, D), cuminaldehyde (4-isopropylbenzaldehyde) was obtained as a secondary product from isomerization–aromatization of the terpene ring, a notable outcome typically seen with Pd catalysts, though POM applications in such reactions are limited.

The catalyst's limitations were apparent with secondary and aliphatic alcohols, which showed low to negligible reactivity.

Case of the SBA-15–$[PEIH]_x[PMo_{12}O_{40}]$ catalyst

Extension towards catalytic dehydration of other carbohydrates. Given the high selectivity of SBA-15–$[PEIH]_x[PMo_{12}O_{40}]$ towards 5-HMF, additional 6-carbon (Scheme 6A) and 5-carbon (Scheme 6B) carbohydrates were evaluated as substrates. Sucrose yielded 5-HMF efficiently within 1 hour, while glucose, an isomer of fructose, only produced a yield of 28%. The one-pot conversion of glucose to 5-HMF involves two steps: isomerization to fructose *via* basic sites (–NH_2 in PEI)[69] and dehydration to 5-HMF catalysed by POMs. Similar systems using MOFs based on Al, Fe and Cr, as well as silicon tungstate-based POMs,[70] have been reported; however, our approach considers molybdenum, a more abundant metal, eliminating the need for additional metal components in the MOF. Finally, cellulose yielded less than 5% due to its strong hydrogen bond network, which hinders product formation. High HMF yields largely depend on the solvent's ability to enhance substrate solubility and stabilize intermediates, particularly when cellulose is used as a feedstock.[71]

For C5 carbohydrates, moderate furfural yields (48–56%) were obtained over extended reaction times (5 h), demonstrating effective substrate-dependent reactivity. For both C5 and C6 carbohydrates, prolonging the reaction time to 20 hours did not improve yields, indicating that optimal conversion occurs within the initial reaction period.

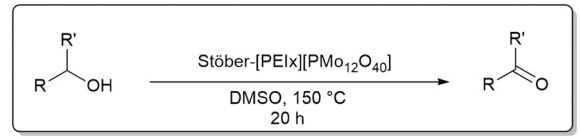

	Substrate	Conv. %	Yield % (Sel. %)
A	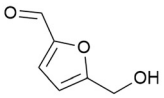	97	86 (90)
B	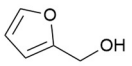	> 99	90 (90)
C	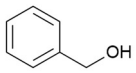	90	85 (95)
D	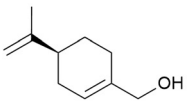	> 99	19 (20)
E	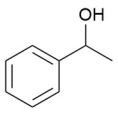	38	38 (100)
F	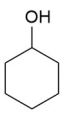	10	10 (100)
G	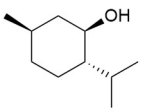	1	n.d (n.d)
H	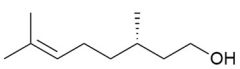	38	<1 (n.d.)

Scheme 5 Stöber–$[PEIH]_x[PMo_{12}O_{40}]$ catalysed alcohol oxidation. Reaction conditions: 0.22 mmol substrate, 4.5 mg Stöber–$[PEIH]_x[PMo_{12}O_{40}]$ (0.05 mol% $PMo_{12}O_{40}$, 0.55 mol% Mo), 1.2 mL of DMSO-d_6, 6.5 mg of naphthalene as the internal standard. Conv. and yields were determined by ^{1}H NMR.

To highlight the significance of this work, a systematic comparison was conducted between a conventional method of DFF synthesis and the selective oxidation of readily available and inexpensive D-fructose as well 5-HMF. For this comparison, five parameters based on green chemistry principles were considered[72] (detailed description is provided in the SI: Fig. S23 and S24 and Table S4). The radial graph in Fig. S24 shows that the atom economy and stochiometric

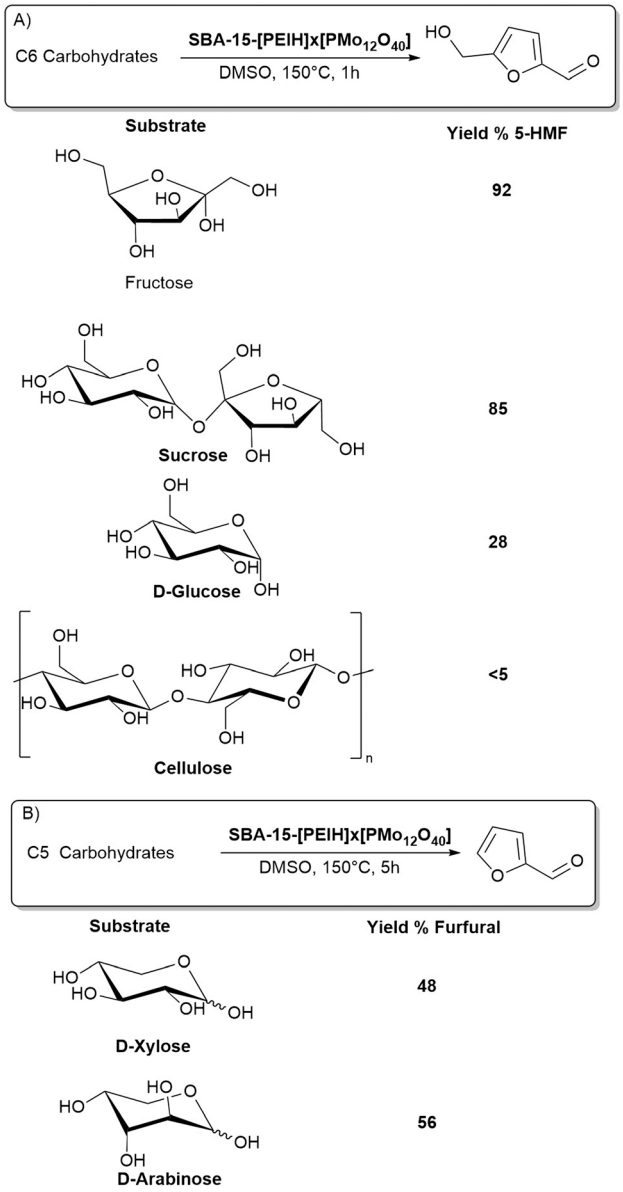

Scheme 6 SBA-15–$[PEIH]_x[PMo_{12}O_{40}]$ catalysed C6 (A) and C5 (B) carbohydrates into 5-HMF or furfural. Reaction conditions: 0.22 mmol substrate, 4.5 mg SBA-15–$[PEIH]_x[PMo_{12}O_{40}]$ (0.05 mol% $PMo_{12}O_{40}$, 0.55 mol% Mo), 1.2 mL of DMSO-d_6, 6.5 mg of naphthalene as the internal standard. Conv. and yields were determined by ^{1}H NMR.

factor are clearly in favour of the catalytic oxidation present in this work.

Conclusions

SiO_2–$[PEIH]_x[PMo_{12}O_{40}]$ materials have demonstrated significant potential as heterogeneous catalysts for the conversion of biomass-derived carbohydrates. Spectroscopic characterization confirms the strong electrostatic interactions between POM clusters and SiO_2–PEI materials, leading to partial reduction of the metal cluster and the formation of Mo(v) species, which play a key role in catalytic performance.

Those materials exhibited different reactivity patterns in the dehydration reaction of D-fructose. The SBA-15–$[PEIH]_x[PMo_{12}O_{40}]$ material provided greater control over side products and achieved a higher 5-HMF yield, attributed to the confinement of POM clusters within the mesoporous structure. In contrast, the Stöber-based material displayed an outstanding turnover number (TON) of 1720, surpassing previously reported catalysts. This remarkable activity is linked to the partial reduction of POMs, facilitated by primary and secondary amines through a photochromic redox process, generating mixed-valence Mo^{6+}/Mo^{5+} species that enhance catalytic efficiency. The reuse of the catalytic material is possible; however, deactivation is attributed to a decrease in the ratio of mixed valence species, which acts as the primary factor limiting catalytic performance.

Overall, the unique redox behaviour and structural properties of the SiO_2–$[PEIH]_x[PMo_{12}O_{40}]$ materials position them as promising candidates for biomass valorisation, offering tunable catalytic activity depending on the support architecture and reaction conditions.

Experimental

Materials and methods

All reagents were acquired from commercial suppliers and used as received (Sigma Aldrich). Micro analysis of the synthesized materials was carried out at USAII ("Unidad de Servicios de Apoyo a la Investigación y a la Industria" (USAII) of Faculty of Chemistry, UNAM) and/or analysis service of "Laboratoire de Chimie de Coordination" (LCC-CNRS). DMSO was dried employing 3 Å molecular sieves and stored under nitrogen. Infrared spectra were recorded on a Perkin-Elmer FTIR/FIR Spectrum 400 spectrometer. ^{1}H and $^{13}C\{^1H\}$ NMR spectra were recorded on a Varian VNMRS spectrometer at 9.4 T (400.13 MHz for ^{1}H), and chemical shifts (δ, ppm) were calibrated relative to the residual solvent peak. Elemental analysis was performed on a Perkin-Elmer 2400 elemental analyzer for CHNS using cysteine as the calibration compound. Thermogravimetric (TGA) data were recorded on a Perkin-Elmer TGA 4000 analyzer from room temperature to 600 °C with a speed of 5 °C min^{-1}. Metal content was established by inductively coupled plasma optical emission spectroscopy (ICP-OES) performed at the "Laboratoire de Chimie de Coordination, Toulouse" using a Thermo Scientific ICAP 6300 instrument equipped with a unique charge injection device (CID) detector, and samples were solubilized by acid etching before analysis.

Electronic spectra were measured over the range of 40 000–5000 cm^{-1} by the diffuse reflectance method on a Cary-5000 Varian spectrophotometer at room temperature.

For surface area analysis, a Micromeritics TriStar 3000 surface area and pore size analyzer was used to produce nitrogen physisorption isotherms at 77 K on synthesized materials. The data were fitted using a Brunauer–Emmett–Teller (BET) model to determine the apparent surface areas of the materials. The average pore diameter and cumulative

pore volumes were calculated using the Barrett–Joyner–Halenda (BJH) model for mesopores. The samples were degassed under vacuum at 130 °C for 18 h prior to the analysis. The scanning electron microscopy (SEM) micrographs of the synthesized materials were obtained on a JEOL JSM-5900-LV microscope. The particle diameter was determined by counting at least 100 individual particles with the software package Digimizer 4.6.1.[73]

EPR measurements were made at 77 K using liquid nitrogen in quartz tubes with a Jeol JES-TE300 spectrometer operating at X band frequency (9.4 GHz) at a 100 kHz field modulation with a cylindrical cavity (TE011 mode). The external measurement of the static magnetic field was made with a Jeol ES-FC5 precision gaussmeter.

Catalytic reactions were performed using a Radleys® parallel reactor system. Catalytic conversions were determined on a Varian 3800 gas chromatograph with a capillary column DB-WAX (30 m × 0.32 mm × 0.25 mm) coupled to an FID detector, using naphthalene as the internal standard.

Solid-state NMR experiments were recorded at the LCC (Toulouse) on a Bruker Avance 400 spectrometer equipped with 2.5, 3.2 or 4 mm probes. Samples were packed into 4 mm zirconia rotors. The rotors were spun at 8 kHz at 293 K. ^{13}C CP-MAS, ^{29}Si UDEFT-MAS and ^{31}P CP-MAS spectra were recorded with a recycling delay of 2 s and contact times of 3 ms or 4 ms. NMR spectra were fitted using the DMfit software.[74]

The synthesis of SBA-15 followed a protocol reported by Zhao *et al.*[41] The template was removed by calcination at 550 °C in air for 5 h, and the resulting synthesized rod-shaped mesoporous silica was denoted as SBA-15. The synthesis of Stöber silica followed literature reports elsewhere,[42,75] the solid obtained was treated with a mixture of 10 mL H_2SO_4 : HNO_3 (5 : 1) and refluxed overnight. The solution was filtered, and the white powder was washed with copious amounts of distilled H_2O until neutral pH was reached and dried under vacuum at 80 °C for 24 h. The resulting as-synthesized spherical silica was denoted as Stöber.

Silica functionalization with PEI_{600}. The silicas (SBA-15 and Stöber) were molecularly modified by a post-synthetic methodology.[44] SiO_2 (SBA-15 or Stöber, 3.0 g, vacuum-dried at 150 °C overnight before use) was initially dispersed in dry toluene (100 mL) under a nitrogen atmosphere. 3-Chloropropyltriethoxysilane (3 g, 12.45 mmol, 3 mL) was added to the suspension, and the mixture was heated at 150 °C for 24 h under nitrogen. The resulting solid was recovered by filtration through Whatman No. 5 filter paper and washed successively with abundant amounts of toluene, petroleum ether, methanol, and diethyl ether. Finally, the white powder (SiO_2–Cl) was dried under a Schlenk line vacuum at 100 °C overnight.

PEI_{600} (9.0 g, previously vacuum-dried at 80 °C overnight before use) was fully dissolved in distilled H_2O (6.0 g) and ethanol (100 mL). The solution was then degassed with N_2 for 30 min. The propyl chloride material (SiO_2–Cl) was introduced into the solution under nitrogen and sonicated at room temperature for 30 min. Subsequently, the mixture was stirred at 90 °C for 24 h under N_2. The resulting material was recovered by filtration (Whatman No. 5) and washed three times with distilled H_2O, twice with an ammonia solution (28 wt%, approximately 50 mL), three times again with H_2O, and twice with methanol before being dried under vacuum at around 80 °C overnight, affording SBA-15–PEI or Stöber–PEI as a fine yellowish-white solid.

General procedure for the synthesis of SiO_2–$[PEIH_x][PMo_{12}O_{40}]$. SiO_2–PEI (SBA-15 or Stöber, 1.0 g, vacuum-dried at 80 °C overnight before use) was initially dispersed in 25 mL of MeCN, under vigorous magnetic agitation. $H_3[PMo_{12}O_{40}]\cdot 25H_2O$ (0.05 mmol, 114 mg) was added turning the yellow compound slowly to a blue suspension. The mixture was stirred at room temperature (*ca.* 20 °C) for 24 h. The resulting blue solid was recovered by vacuum filtration (Fritted glass) and washed three times with MeCN and 3 times with distilled H_2O before being dried under vacuum at around 80 °C overnight affording blue solids.

General procedure for one-pot catalytic D-fructose valorisation. In the Radleys® parallel reactor system, a glass tube equipped with magnetic stirring was charged with 65 mg of naphthalene in 6 mL of dry DMSO, and the mixture was heated to 150 °C. D-Fructose (200 mg, 1.11 mmol) and the catalyst (11.3, 22.5 or 45 mg) were added in one portion to the pre-heated mixture. 200 μL of the reaction mixture was withdrawn periodically, diluted in 2 mL of MeCN, passed through a syringe filter (PTFE, 0.45 μm) and injected for GC-FID o GC-MS analysis.

General procedure for recycling experiments of D-fructose dehydration by SBA-15–$[PEIH]_x[PMo_{12}O_{40}]$. In the Radleys® parallel reactor system, a glass tube equipped with magnetic stirring was charged with 65 mg of naphthalene in 6 mL of dry DMSO and heated to 150 °C. D-Fructose (200 mg, 1.11 mmol) and SBA-15–$[PEIH]_x[PMo_{12}O_{40}]$ (22.5 mg) were added in a single portion to the pre-heated mixture. After the reaction, the catalyst was separated by centrifugation at 4000 rpm for 30 minutes. The liquid phase was decanted for GC analysis, and the recovered solid was washed twice with 3 mL of MeCN and then vacuum-dried at 80 °C overnight. The reaction procedure was repeated, and, in the final run, 10 mg of the recovered catalyst was analysed by TEM.

General procedure for carbohydrate valorisation to 5-HMF with SBA-15–$[PEIH]_x[PMo_{12}O_{40}]$. In a vial, 0.22 mmol of substrate, 4.5 mg of SBA-15–$[PEIH]_x[PMo_{12}O_{40}]$ (11.3 wt%), and 6.5 mg of naphthalene in 1.2 mL of DMSO-d_6 were sonicated for 5 min. The mixture was quantitatively transferred to an NMR tube which was then placed in a preheated sand bath at 150 °C for 1 or 5 h. After the reaction time, the tube was cooled with water, and the products were analysed by ^1H NMR spectroscopy; the conversion and yields are the average of 2 runs.

General procedure for alcohol oxidation with Stöber–$[PEIH]_x[PMo_{12}O_{40}]$. In a vial, 0.22 mmol of alcohol, 4.5 mg of Stöber–$[PEIH]_x[PMo_{12}O_{40}]$ (11.3 wt%), and 6.5 mg of naphthalene in 1.2 mL of DMSO-d_6 were sonicated for 5 min.

The mixture was quantitatively transferred to an NMR tube which was then placed in a preheated sand bath at 150 °C for 20 h. After the reaction time, the tube was cooled with water, and the products were analysed by ^{1}H NMR spectroscopy; the conversion and yields are the average of 2 runs.

Author contributions

ITPD: investigation, formal analysis, methodology, visualization, conceptualization, and writing – original draft; IGR: conceptualization, funding acquisition, project administration, supervision, visualization, resources, and writing – review & editing; DA: project administration, conceptualization, funding acquisition, supervision, visualization, resources, and writing – review & editing.

Conflicts of interest

The authors declare no competing financial interest.

Data availability

Full characterization of materials (solid NMR, IR, N_2 isotherms, TGA, elemental analysis and PXRD analysis) and selected catalytic experiments. See DOI: **https://doi.org/10.1039/D5CY00465A**.

The data supporting this article have been included as part of the SI.

Acknowledgements

I. T. P.-D. thanks SECIHTI (CVU: 954059), IFAL- Ambassade de France au Mexique and EUR grant NanoX n° ANR-17-EURE-0009 in the framework of the Programme des Investissements d'Avenir for fellowship and mobility PhD grants. All authors thank UNAM DGAPA-PAPIIT IN222424 and SECIHTI through grant CBF2023-2024-766 for financial support. Dr. Yannick Coppel, Sandrine Vincendeau and Dr. Karla P. Salas-Martin are warmly acknowledged for their technical support. All authors thank LCC-CNRS, Université de Toulouse, CNRS, UPS, Toulouse, France for financial support and for the solid NMR facilities and IUT-Chem. Dpt. for the equipment facilities.

References

1 L. Szabó, R. Milotskyi, G. Sharma and K. Takahashi, *Green Chem.*, 2023, **25**, 5338–5389.
2 L. T. Mika, E. Cséfalvay and Á. Németh, *Chem. Rev.*, 2018, **118**, 505–613.
3 Z. Zhang and G. W. Huber, *Chem. Soc. Rev.*, 2018, **47**, 1351–1390.
4 C. Chatterjee, F. Pong and A. Sen, *Green Chem.*, 2015, **17**, 40–71.
5 T. Wang, M. W. Nolte and B. H. Shanks, *Green Chem.*, 2014, **16**, 548–572.
6 A. Shrotri, H. Kobayashi and A. Fukuoka, *Acc. Chem. Res.*, 2018, **51**, 761–768.
7 L. Hu, Z. Wu, Y. Jiang, X. Wang, A. He, J. Song, J. Xu, S. Zhou, Y. Zhao and J. Xu, *Renewable Sustainable Energy Rev.*, 2020, **134**, 110317.
8 R.-J. Van Putten, J. C. Van Der Waal, E. De Jong, C. B. Rasrendra, H. J. Heeres and J. G. De Vries, *Chem. Rev.*, 2013, **113**, 1499–1597.
9 K. Gupta, R. K. Rai and S. K. Singh, *ChemCatChem*, 2018, **10**, 2326–2349.
10 L. Hu, L. Lin, Z. Wu, S. Zhou and S. Liu, *Renewable Sustainable Energy Rev.*, 2017, **74**, 230–257.
11 H. Wang, C. Zhu, D. Li, Q. Liu, J. Tan, C. Wang, C. Cai and L. Ma, *Renewable Sustainable Energy Rev.*, 2019, **103**, 227–247.
12 W. Liang, R. Zhu, X. Li, J. Deng and Y. Fu, *Green Chem.*, 2021, **23**, 6604–6613.
13 G. Lv, H. Wang, Y. Yang, T. Deng, C. Chen, Y. Zhu and X. Hou, *ACS Catal.*, 2015, **5**, 5636–5646.
14 S.-S. Wang and G.-Y. Yang, *Chem. Rev.*, 2015, **115**, 4893–4962.
15 I. A. Weinstock, R. E. Schreiber and R. Neumann, *Chem. Rev.*, 2018, **118**, 2680–2717.
16 A. Enferadi-Kerenkan, T.-O. Do and S. Kaliaguine, *Catal. Sci. Technol.*, 2018, **8**, 2257–2284.
17 J. Zhong, J. Pérez-Ramírez and N. Yan, *Green Chem.*, 2021, **23**, 18–36.
18 A. R. Gaspar, J. A. F. Gamelas, D. V. Evtuguin and C. Pascoal Neto, *Green Chem.*, 2007, **9**, 717.
19 N. Narkhede, S. Singh and A. Patel, *Green Chem.*, 2015, **17**, 89–107.
20 W. Deng, Q. Zhang and Y. Wang, *Dalton Trans.*, 2012, **41**, 9817.
21 A. S. Chauhan, A. Kumar, R. Bains and P. Das, *Green Chem.*, 2022, **24**, 6125–6130.
22 R. Liu, J. Chen, L. Chen, Y. Guo and J. Zhong, *ChemPlusChem*, 2014, **79**, 1448–1454.
23 Y. Liu, L. Zhu, J. Tang, M. Liu, R. Cheng and C. Hu, *ChemSusChem*, 2014, **7**, 3541–3547.
24 W. Zhang, H. Qian, Q. Hou and M. Ju, *Green Chem.*, 2023, **25**, 893–914.
25 A. Misra, K. Kozma, C. Streb and M. Nyman, *Angew. Chem., Int. Ed.*, 2020, **59**, 596–612.
26 A. S. Cherevan, S. P. Nandan, I. Roger, R. Liu, C. Streb and D. Eder, *Adv. Sci.*, 2020, **7**, 1903511.
27 Y. Li, P. Li, P. Cao, Y. Li, X. Wang and S. Wang, *ChemSusChem*, 2019, **12**, 3515–3523.
28 D. Liu, B. Chen, J. Li, Z. Lin, P. Li, N. Zhen, Y. Chi and C. Hu, *Inorg. Chem.*, 2021, **60**, 3909–3916.
29 A. Dolbecq, E. Dumas, C. R. Mayer and P. Mialane, *Chem. Rev.*, 2010, **110**, 6009–6048.
30 L. Hombach, N. Simitsis, J. T. Vossen, A. J. Vorholt and A. K. Beine, *ChemCatChem*, 2022, **14**, e202101838.
31 B. J. S. Johnson and A. Stein, *Inorg. Chem.*, 2001, **40**, 801–808.
32 Q. Wang, Y. Li, H. Guan, H. Yu and X. Wang, *ChemPlusChem*, 2021, **86**, 997–1005.
33 Y. Sun, J. Zheng, J. Xu, K. Yang, Z. Zhu, T. Su, H. Ge, W. Ren and H. Lü, *Fuel*, 2022, **315**, 123226.

34 M. Gong, W.-X. Mu, Y.-D. Cao, Y.-W. Shao, X. Hu, D. Yin, H. Liu, C.-H. Zhang and G.-G. Gao, *Fuel Process. Technol.*, 2023, **242**, 107635.
35 Q. Wang, W. Bu, Z. Li, Y. Qi and X. Wang, *Chin. Chem. Lett.*, 2023, **34**, 107548.
36 E. Grinenval, X. Rozanska, A. Baudouin, E. Berrier, F. Delbecq, P. Sautet, J.-M. Basset and F. Lefebvre, *J. Phys. Chem. C*, 2010, **114**, 19024–19034.
37 A. Galván, E. Damian-Ascencio, M. Martínez, J. M. Domínguez-Esquivel and M. A. Vázquez, *New J. Chem.*, 2023, **47**, 8258–8267.
38 H. Wang, M. Wang, J. Shang, Y. Ren, B. Yue and H. He, *Materials*, 2020, **13**, 507.
39 S. Yan, Y. Li, P. Li, T. Jia, S. Wang and X. Wang, *RSC Adv.*, 2018, **8**, 3499–3511.
40 E. Grinenval, F. Bayard, J.-M. Basset and F. Lefebvre, *Inorg. Chem.*, 2014, **53**, 2022–2029.
41 D. Zhao, Q. Huo, J. Feng, B. F. Chmelka and G. D. Stucky, *J. Am. Chem. Soc.*, 1998, **120**, 6024–6036.
42 Y. Wang, F. Gayet, P. Guillo and D. Agustin, *Materials*, 2019, **12**, 3278.
43 Y. Han, Z. Lu, Z. Teng, J. Liang, Z. Guo, D. Wang, M.-Y. Han and W. Yang, *Langmuir*, 2017, **33**, 5879–5890.
44 W. Long, N. A. Brunelli, S. A. Didas, E. W. Ping and C. W. Jones, *ACS Catal.*, 2013, **3**, 1700–1708.
45 I. T. Pulido-Díaz, A. Serrano-Maldonado, C. C. López-Suárez, P. A. Méndez-Ocampo, B. Portales-Martínez, A. Gutiérrez-Alejandre, K. P. Salas-Martin and I. Guerrero-Ríos, *Dalton Trans.*, 2021, **50**, 3289–3298.
46 N. T. Duong, J. Trébosc, O. Lafon and J.-P. Amoureux, *Solid State Nucl. Magn. Reson.*, 2019, **100**, 52–62.
47 I. S. Protsak, Y. M. Morozov, W. Dong, Z. Le, D. Zhang and I. M. Henderson, *Nanoscale Res. Lett.*, 2019, **14**, 160.
48 D. R. Holycross and M. Chai, *Macromolecules*, 2013, **46**, 6891–6897.
49 T. Yamase, *Chem. Rev.*, 1998, **98**, 307–326.
50 D. Amitouche, M. Haouas, T. Mazari, S. Mouanni, R. Canioni, C. Rabia, E. Cadot and C. Marchal-Roch, *Appl. Catal., A*, 2018, **561**, 104–116.
51 R. I. Maksimovskaya, *Polyhedron*, 2013, **65**, 54–59.
52 E. Ishikawa and T. Yamase, *Bull. Chem. Soc. Jpn.*, 2000, **73**, 641–649.
53 G. S. Armatas, G. Bilis and M. Louloudi, *J. Mater. Chem.*, 2011, **21**, 2997.
54 D. Carriazo, C. Domingo, C. Martín and V. Rives, *J. Solid State Chem.*, 2008, **181**, 2046–2057.
55 T. Rui Zhang, W. Feng, R. Lu, C. Yan Bao, T. Jin Li, Y. Ying Zhao and J. Nian Yao, *J. Solid State Chem.*, 2002, **166**, 259–263.
56 C. Sanchez, J. Livage, J. P. Launay, M. Fournier and Y. Jeannin, *J. Am. Chem. Soc.*, 1982, **104**, 3194–3202.
57 J. Lu, X. Zhang, P. Ma, V. Singh, C. Zhang, J. Niu and J. Wang, *J. Mater. Sci.*, 2018, **53**, 3078–3086.
58 Z. Chen, B. H. Loo, Y. Ma, Y. Cao, A. Ibrahim and J. Yao, *ChemPhysChem*, 2004, **5**, 1020–1026.
59 J. Wu, S. Yan, C. Wang, C.-H. Lay, X. Wang, X. Wang and M. Huo, *Chemosphere*, 2021, **277**, 130316.
60 A. Ranoux, K. Djanashvili, I. W. C. E. Arends and U. Hanefeld, *ACS Catal.*, 2013, **3**, 760–763.
61 D. W. Brown, A. J. Floyd, R. G. Kinsman and Y. Roshanhyphen;Ali, *J. Chem. Technol. Biotechnol.*, 1982, **32**, 920–924.
62 J. Zhang, M. Sun, X. Liu and Y. Han, *Catal. Today*, 2014, **233**, 77–82.
63 R. Wölfel, N. Taccardi, A. Bösmann and P. Wasserscheid, *Green Chem.*, 2011, **13**, 2759.
64 I. Van Zandvoort, E. J. Koers, M. Weingarth, P. C. A. Bruijnincx, M. Baldus and B. M. Weckhuysen, *Green Chem.*, 2015, **17**, 4383–4392.
65 L. Liu, in *Biomass-Derived Humins*, Springer Nature Singapore, Singapore, 2023, pp. 7–21.
66 M. Chalid, H. J. Heeres and A. A. Broekhuis, *J. Appl. Polym. Sci.*, 2012, **123**, 3556–3564.
67 A. M. Khenkin and R. Neumann, *J. Org. Chem.*, 2002, **67**, 7075–7079.
68 R. Tyburski, T. Liu, S. D. Glover and L. Hammarström, *J. Am. Chem. Soc.*, 2021, **143**, 560–576.
69 Q. Yang and T. Runge, *ACS Sustainable Chem. Eng.*, 2016, **4**, 6951–6961.
70 M. Lara-Serrano, S. Morales-delaRosa, J. M. Campos-Martin, V. K. Abdelkader-Fernández, L. Cunha-Silva and S. S. Balula, *Adv. Sustainable Syst.*, 2022, **6**, 2100444.
71 H. Wu, R. Zhang, Y. Zhai, X. Song, J. Xiong, X. Li, Y. Qiao, X. Lu and Z. Yu, *ChemSusChem*, 2023, **16**, e202201809.
72 J. Andraos and M. Sayed, *J. Chem. Educ.*, 2007, **84**, 1004.
73 *Digimizer (version 4.6.1) MedCalc Software*, Belgium, 2005.
74 D. Massiot, F. Fayon, M. Capron, I. King, S. Le Calvé, B. Alonso, J. Durand, B. Bujoli, Z. Gan and G. Hoatson, *Magn. Reson. Chem.*, 2002, **40**, 70–76.
75 W. Dexuan, L. Guian, H. Qingyan, W. Ziqiang, P. Liping, Z. Zhongyue and Z. Hairong, *J. Nanosci. Nanotechnol.*, 2016, **16**, 3821–3826.

